Mon. Not. R. Astron. Soc. **263,** 416–424 (1993)

A search for arcmin-scale anisotropy in the cosmic microwave background

Ravi Subrahmanyan,[1]★ R. D. Ekers,[1] Malcolm Sinclair[1] and Joseph Silk[2]
[1]*Australia Telescope National Facility, CSIRO, PO Box 76, Epping, NSW 2121, Australia*
[2]*Departments of Astronomy and Physics, and Center for Particle Astrophysics, University of California, Berkeley, CA 94720, USA*

Accepted 1993 January 22. Received 1993 January 21; in original form 1992 November 2

ABSTRACT

The Australia Telescope antenna array has been used in an ultracompact configuration to image an ≈8 arcmin diameter field with an angular resolution of about 2 arcmin and an rms brightness sensitivity of about 36 μK. Interferometer spacings which responded to an independent and higher range of spatial frequencies were used to model and subtract the confusion due to the discrete radio sources in the field with smaller angular sizes. As a result, the sensitivity in the imaging was reduced well below the telescope confusion limit. The residual image was examined for fluctuations above the instrument thermal noise that could be due to any arcmin-scale anisotropy in the cosmic microwave background. No excess fluctuations were detected, and we derive a 95 per cent confidence upper limit of 22 μJy beam^{-1} on the rms flux density fluctuations in the background sky at 8.7 GHz with an angular scale of 2 arcmin. Assuming a Gaussian form for the autocorrelation function of the CMB fluctuations, we obtain a 95 per cent confidence limit of $\Delta T/T < 2 \times 10^{-5}$ on the rms fractional temperature fluctuations in a background with a coherence scale of 1 arcmin.

Key words: methods: observational – galaxies: formation – cosmic microwave background – cosmology: observations.

1 INTRODUCTION

The general-relativistic hot big bang cosmology is the best description we have today of the structure of the Universe and its temporal evolution on large scales, where assumptions of homogeneity and isotropy are valid (Peebles et al. 1991). This 'standard' theory predicts an isotropic cosmic microwave background (CMB) with a Planck spectrum as a relict of the radiation era in the early Universe. Although there is not yet a successful theory for the formation of galaxies and their spatial distribution structures, they are usually hypothesized as having formed by the gravitational growth of primordial density perturbations (Peebles & Silk 1990). The coupling of these perturbations to the radiation field is inevitable, and consequently most theories for the origin of galaxies predict anisotropy in the CMB.

The *COBE* detection of CMB anisotropy on angular scales exceeding 7° (Smoot et al. 1992) is possibly a measurement of the spectrum of gravitational potential fluctuations on comoving scales exceeding $750(\Omega h)^{-1}$ Mpc at the surface of last scattering (Ω is the total density parameter, and h is the Hubble constant in units of 100 km s^{-1} Mpc^{-1}). The two-point correlation length that characterizes galaxy clustering today is much smaller and is about $5\,h^{-1}$ Mpc. Anisotropy on the relatively small angular scale of 3Ω arcmin is expected to be the signature of the seeds for mass fluctuations on this scale. The nature of the continuation of the *COBE* spectrum to these smaller scales would be a probe of the seeds for galaxies and structures in galaxy distribution, but arcmin-scale fluctuations in the CMB are yet to be detected.

The density fluctuations, which are believed to be the seed for the formation of structures in the Universe, couple to the relict radiation and generate the primary anisotropies prior to the recombination of the primeval plasma. The recombination phase-transition takes place over a finite cosmic time, however, and therefore the observable amplitudes of these anisotropies are expected to be progressively diminished below an angular scale of about $8\,\Omega^{1/2}\,h^{-1}$ arcmin (Vittorio & Silk 1984). Re-ionization of the baryonic content of the Universe due to energy release in late non-linear evolution

★On leave from the Tata Institute of Fundamental Research, Homi Bhabba Road, Bombay, 400005, India.

will result in a secondary generation of anisotropies. Thomson scattering of the CMB photons off incoherent thermal fluctuations and coherent bulk flows in ionized matter (Ostriker & Vishniac 1986) and the inverse-Compton scattering of the photons by gas heated in gravitational potential wells (Cole & Kaiser 1988; Schaeffer & Silk 1988) are expected to cause secondary anisotropies with specifically arcmin-scale coherence.

Observational constraints on the arcmin-scale anisotropy in the CMB are a test of theories for (i) the primordial mass fluctuation spectrum that seeds galaxy clustering structure and (ii) the secondary processes just described. In an attempt to detect CMB anisotropy on small angular scales, we have made observations using the Australia Telescope Compact Array (ATCA) in a very compact configuration that provides high sensitivity to arcmin-scale brightness temperature fluctuations on the sky. In the next section, we describe our observing strategies and their specific advantages. The following sections describe the observations, the strategy for removing discrete radio sources and the derivation of constraints on arcmin-scale anisotropy in the CMB from an image of high brightness sensitivity.

2 OBSERVING STRATEGIES

2.1 Imaging CMB anisotropies with Fourier synthesis telescopes

The most sensitive limits to date on arcmin-scale anisotropy in the CMB have been placed by observations with the OVRO 40-m telescope using a 'double-switching' technique to minimize systematic errors (Readhead et al. 1989). The main factors limiting the sensitivity of such a beam-switching experiment with a single dish are (i) differential atmospheric emission and ground spillover contributions and (ii) confusion due to radio sources in the sky. The NRAO Very Large Array (VLA) has been used in a Fourier synthesis imaging mode to place upper limits on arcmin- and subarcmin-scale fluctuations with a similar sensitivity (Fomalont et al. 1992). Interferometers respond only to specific spatial frequencies, and therefore they are insensitive to any uniform sky brightness as well as to atmospheric emission anisotropies (even if time-variable) on scales greater than the interferometer beam pattern. Also, interferometers filter out signals which appear at the antennas with a fringe rate different from that towards the phase-tracking centre, making them relatively insensitive to ground spillover, terrestrial interference and systematics generated within the telescope electronics. As detailed in Section 2.3, these can all be avoided by placing the phase-tracking centre well offset from the sky region of interest. The relative immunity of an interferometer from systematic errors makes it an attractive instrument for sensitive observations requiring very long integrations.

The range of instantaneous baselines in an interferometer array provides simultaneous measurements of sky-brightness fluctuations over a range of coherence scales. A synthesis telescope provides an *image* of the sky rather than difference measurements, and this makes it easier to relate theoretical models for CMB anisotropy to the observational results. Moreover, since the measurements are made in the Fourier transform visibility domain, the instrumental thermal-noise characteristics can be well determined from the data, and various checks can be performed to confirm the reality of any detected signals. Perhaps the most important advantage in making measurements of CMB fluctuations with a synthesis telescope is that the longer interferometer spacings, which involve the same antennas and therefore suffer exactly the same calibration errors as the shorter spacings, can be used to subtract the response to discrete foreground sources from the visibility data of the short interferometer spacings with high accuracy. This allows a search for CMB fluctuations on scales corresponding to the short spacings without confusion from foreground point-like radio sources.

To summarize, a Fourier synthesis instrument is relatively free of systematic errors and also offers several advantages over experiments with single dishes. For these reasons, we have initiated a programme for arcmin-resolution imaging of CMB anisotropies using the Australia Telescope Compact Array.

2.2 Observing efficiency

Analogous to the definition for the antenna temperature of a single dish (see equation 3-116 in Kraus 1986), we define the 'antenna temperature' of a synthesis telescope due to a sky-brightness distribution $T_{\rm sky}(\theta, \phi)$ as

$$T_{\rm a} = \eta_{\rm a} \frac{\int\int T_{\rm sky}(\theta,\phi) B_{\rm p}(\theta,\phi) B_{\rm s}(\theta,\phi)\, {\rm d}\theta\, {\rm d}\phi}{\int\int B_{\rm p}(\theta,\phi)\, {\rm d}\theta\, {\rm d}\phi}, \qquad (1)$$

where $\eta_{\rm a}$ represents the antenna aperture efficiency, and $B_{\rm p}(\theta, \phi)$ and $B_{\rm s}(\theta, \phi)$ represent the normalized power patterns of the primary and synthesized beams respectively. The images are optimally sensitive to sky fluctuations on the scale of the synthesized beam. Since the synthesized beam is generally much smaller than the primary beam, the fluctuations in the 'antenna temperature' of the array (when the synthesized beam scans the sky) would be less than the sky-temperature fluctuations on the scale of the synthesized beam by approximately the antenna aperture efficiency, times the ratio of the synthesized and primary beam solid angles, i.e., $\Delta T_{\rm a} \approx \eta_{\rm a}(\Omega_{\rm s}/\Omega_{\rm p})\Delta T_{\rm sky}$.

The rms instrument noise $\Delta T_{\rm n}$ in the measurement of this 'antenna temperature' is given by $T_{\rm sys}/\sqrt{2B\tau M}$, where $T_{\rm sys}$ is the telescope system temperature, B the observing bandwidth, τ the integration time and M the total number of independent visibility measurements that go into making the image (Thompson, Moran & Swenson 1986).

We may define the observing efficiency by the product of the signal-to-noise ratio with which a sky fluctuation is detectable (the brightness sensitivity) times the square root of the number of independent measurements of the sky brightness:

$$\xi = \frac{(\Delta T_{\rm a}/\Delta T_{\rm n})}{\Delta T_{\rm sky}} \sqrt{l}\,. \qquad (2)$$

The number of independent measurements on the sky is approximately the ratio of the primary-to-synthesized beam solid angles, i.e. $l = (\Omega_{\rm p}/\Omega_{\rm s})$. When the array is made compact and the antennas are moved closer, the synthesized beam

solid angle increases. The brightness sensitivity improves but the number of independent image pixels decreases. The net effect is to increase the observing efficiency, so the most efficient array configuration is one where the antennas are closely packed with the projected antenna spacing nearly equal to their diameters.

For an east–west array with m antennas in such a closely packed configuration, the synthesized beam solid angle (after a full Earth-rotation synthesis observation of a high-declination field) will be approximately a factor m^2 less than that of the primary beam. The observing efficiency of the array would equal approximately that of a single dish. However, if the image were synthesized at a lower resolution using only the spacings between adjacent antennas, the observing efficiency of the array would improve by a factor $\sqrt{m}$ and would then be similar to the observing efficiency of m independent single dishes.

2.3 Observing strategy with the Australia Telescope

The Australia Telescope Compact Array (see The Australia Telescope 1992) is a Fourier-synthesis telescope consisting of an array of five 22 m diameter dish-type antennas on a 3-km-long east–west railtrack. A sixth antenna is located 3 km to the west of the western end of the railtrack. The five antennas are movable and can be located on any of 35 stations along the railtrack; adjacent antennas can be placed at a closest distance of 30.612 m. The telescope operates in bands located around wavelengths of 20, 13, 6 and 3.5 cm. Continuum observations can be made in both orthogonal polarizations with a multi-channel mode using a pair of 128-MHz-wide bands. To maximize the observing efficiency in the search for CMB fluctuations, an ultracompact array configuration was used, in which all five antennas on the 3-km railtrack were located on stations spaced 30.612 m apart.

If the telescope system temperature were the same at all wavelength bands, observations with our optimal array configuration at different frequencies would measure CMB brightness-temperature fluctuations on different scales with the same sensitivity. The ATCA electronics currently have lower T_{sys} at longer wavelengths, but our observations in the compact configuration are primarily limited by confusion due to the discrete foreground radio sources in the sky. Over the telescope's present frequency range of operation, confusion is least at the highest operating frequencies (Franceschini et al. 1989), so we made the observations reported here in the 3.5-cm wavelength band despite the somewhat higher receiver noise from the FET amplifiers currently used in this band.

With the 22 m diameter antennas spaced 30.612 m apart on the east–west railtrack, observations at declinations north of $-44°$ would be possible only over a restricted hour-angle range, because adjacent antennas would shadow at large hour angles. The identification and accurate subtraction of discrete sources in the observed fields is easier when the observations are made over a wide hour-angle range and the synthetic beam is roughly circular in shape; this is possible only in observations of fields at high declinations, although observations at higher declinations have smaller synthesized beams and poorer observing efficiency. Since confusion is the primary limiting factor of our experiment, we have chosen to observe at a declination close to $-50°$. The brightness sensitivity would be about 40 per cent higher in fields at a declination of $-50°$ than at $-90°$. For our choice of declination, there is no shadowing of the antennas at any hour angle, and the projected spacing between adjacent antennas is nearly the dish diameter over a large hour-angle range. Interferometry between slightly porous antennas with geometric shadowing produces correlated response to any uniform sky brightness, and our choice of declination avoids this problem.

Systematics within the telescope electronics (e.g. offsets in the digital sampler levels) generally produce artefacts at the observing phase centre. The phase centre is the point on the sky for which the instrument is adjusted to have white-light fringes which are stationary with respect to the sky. These phase-centre errors can be moved outside the region of interest, but this will cause some reduction in image quality due to fringe smearing with the finite time constant and bandwidth. The multi-channel continuum observing mode of the ATCA provides 32 frequency channels spaced 4 MHz apart over the 128-MHz-wide bands. Each channel has a noise equivalent bandwidth of 8 MHz. Considering the longest interferometer spacing of 122.45 m in our compact ATCA configuration, the fractional reduction in the visibility amplitude due to bandwidth smearing within the channel bandwidths would be <1–2 per cent, even if the phase-tracking centre were offset 1° from the field being observed. The attenuation in visibility amplitudes due to the on-line time-averaging smearing will also be within 1 per cent for integration periods of 10 s. Consequently, we were able to make our observations with the phase centre offset about 1° from the antenna pointing centre and therefore about 10 primary beamwidths away from the sky region being imaged. Different phase-centre positions were used on different observing days.

Tests performed with closely located ATCA antennas have not shown any cross-talk at the observing frequencies. The signals are digitized in the vertex rooms at the antennas, eliminating any possibility of signals coupling into the interferometer arms subsequently. The on-axis Cassegrain design of the antenna optics, the low porosity of the reflecting surface and the thinness of the support structure for the secondary reflector are additional design features which reduce the effects of cross-talk in the ATCA. The sampling signals and their harmonics are generated coherently in the antennas, and their coupling to the video signals is the major internally generated spurious correlation. Since the correlator design confines their effects to alternate channels, we have routinely rejected these alternate channels. The noise-equivalent bandwidths of the channels are twice the channel separation, and the alternate channel data are redundant.

The visibility obtained between adjacent antennas is an average of the visibilities between all pairs of aperture elements between the two antennas weighted by the aperture illumination. The brightness sensitivity is enhanced by increasing the contribution from the shortest spacings. The ATCA-dish optics have been designed to have a high illumination out to the dish edge with a sharp cut-off. Although this creates high sidelobe responses in the primary beam pattern, the brightness sensitivity in closely spaced elements is improved.

3 OBSERVATIONS

Since confusion from radio sources is the limiting factor in our observations, we have selected our observing field to be relatively devoid of stronger radio sources. The field of view is defined by the antenna primary beam which has a HPBW of 5.9 arcmin at our observing frequency of 8.7 GHz. Sources lying beyond about 30 arcmin from the field centre will be strongly attenuated by $\gtrsim 50$ dB by the antenna primary beam, with an additional attenuation of $\gtrsim 20$ dB provided by the synthesized beam, off-line time averaging and frequency-channel averaging. Sources within 30 arcmin and outside the main lobe will have lesser attenuation due to the -20 dB level primary beam sidelobes, and therefore the distribution of nearby sources is an important consideration in the choice of the field centre. Using the Molonglo 408-MHz survey (Large et al. 1981) and the Parkes data base (Wright & Otrupcek 1990), we identified a region of about 3° diameter in the vicinity of the South Galactic Pole that was devoid of catalogued radio sources. The survey by Haslam et al. (1982) also showed no extended emission in the region. We mosaic-imaged a 1° field in this region with the ATCA at 20 cm with an rms sensitivity of 0.3 mJy beam^{-1}. On the basis of our measurements of the antenna beam at 8.7 GHz, a field centre was selected so that the maximum response due to the detected sources within 40 arcmin would not exceed 25 μJy (20-cm flux density). No sources exceeding 1 mJy (at 20 cm) are present within the antenna main lobe region. The J2000.0 epoch coordinates of the field centre are RA $03^{h}\ 16^{m}\ 26\overset{s}{.}00$ and Dec. $-49°\ 47'\ 57''.00$. SERC J plates show no optical objects brighter than about 16 mag in the field.

During 1991 July–August, six observations were made of the field in a single band at 8640 MHz. In 1991 December, three more observations were made using a pair of bands at 8640 and 8768 MHz. Each observation consisted of a full Earth-rotation synthesis observation over a 12-h period. Observations were made in dual linear polarizations, using bandwidths of 128 MHz at each frequency. The field was observed in scans of 20 min with a secondary calibrator PKS 0308−611 observed for 3–4 min between scans. PKS 1934−638 was observed once during each of the synthesis observations as a primary flux density calibrator.

Observations of the field and calibrator were made with the phase centre offset ~1°. The first data-reduction step was to correct separately the visibility phases in the channel data for these shifts. Subsequently, the time and frequency dependences of the antenna complex gains were calibrated using the observations of PKS 0308−611, which is an unresolved source in the observing configuration. The overall flux scale was set using the observations of PKS 1934−638, whose flux density was assumed to be 2.59 and 2.52 Jy at 8640 and 8768 MHz respectively. The calibrated multi-channel continuum data were averaged in frequency over the useful bandwidth of 120 MHz in each band. The data were also time-averaged (averaging times decreasing from 52 to 13 min with increasing baseline length) in order to provide additional attenuation to sources outside the field of view. Images were made by gridding and Fourier transforming the visibilities using standard NRAO AIPS routines. The data obtained at the two frequencies were imaged separately, and the images were averaged with weights

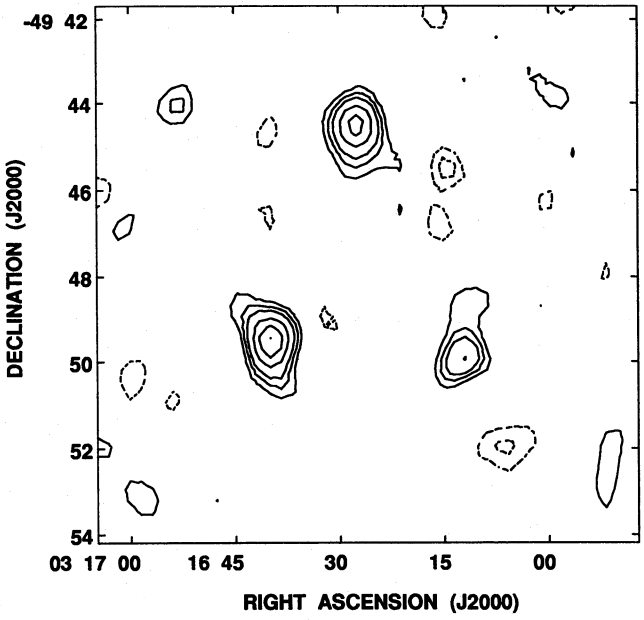

Figure 1. Deconvolved image of the field made using all the baseline data. The components have been restored with a beam of size 68×57 arcsec^2 at a position angle $-6°$. Contours are at -3, -2, 2, 3, 4, 6, 8 and 10×25 μJy beam^{-1}.

proportional to the number of visibility measurements forming each image. A deconvolved image of the field made using all the data is shown in Fig. 1. The image has an rms noise of 25 μJy beam^{-1} in source-free regions.

The observations were made in the most compact ATCA configuration with 4, 3, 2 and 1 baselines with lengths 30.6, 61.2, 91.8 and 122.4 m respectively. Useful integration times of about 70 and 20 h were obtained at 8640 and 8768 MHz respectively. The mean system temperature of the ATCA at these frequencies is currently about 67 K, and the expected thermal rms noise in the image in Fig. 1 is 21 μJy beam^{-1}. An image made using only the four 30.6-m baselines is expected to have an rms instrumental noise of 33 μJy beam^{-1}, while images that use the six longer baselines from 61.2 to 122.4 m will have an rms noise of 27 μJy beam^{-1}.

A lower resolution image of the field (Fig. 2) with higher brightness-sensitivity was made by using the four 30.6-m baseline visibility data. In order to preserve the linear relationship between this image and the real sky, no attempt was made at any deconvolution. The instrumental noise in this image (σ_N), as estimated by imaging regions far from the primary beam, is 33.5 μJy beam^{-1}, as expected from the telescope system temperature. We estimate the variance (σ_I^2) in the image of the sky by computing the weighted average of the squares of the image intensities, using a weighting that is the square of the primary beam pattern. The corresponding rms noise (σ_I) in the image in Fig. 2 is 143 μJy beam^{-1}, and is clearly well above the instrumental noise. We made separate images of the sky using the visibilities in the pair of orthogonal polarizations and differenced them. The difference map had $\sigma_I = 2 \times 30$ μJy beam^{-1}, which is consistent with the expectation from instrumental noise alone, and this suggests that the image in Fig. 2 has an rms noise of about 140 μJy beam^{-1} due to celestial sources. This problem is addressed in the following two sections.

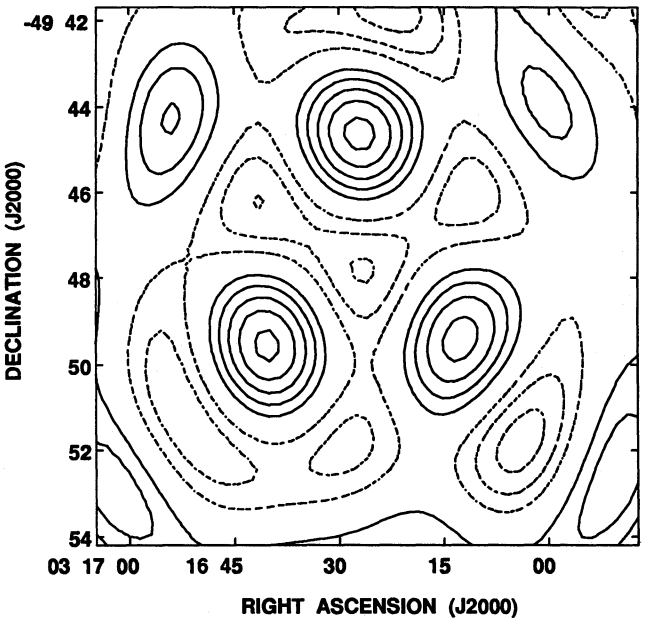

Figure 2. Confusion-limited image of the field made using only the 30.6-m baselines. Contours at $-6, -4, -2, 2, 4, 6, 8$ and 10×33.5 μJy beam^{-1}.

4 FOREGROUND RADIO SOURCES

4.1 An estimate of confusion noise

The average number density of discrete radio sources in the sky exceeding a limiting flux density $S_{\mu Jy}$ μJy has been estimated by Windhorst et al. (1993) to be

$$N(>S_{\mu Jy}) = 19\, S_{\mu Jy}^{-1.3} \text{ arcmin}^{-2} \quad (3)$$

close to our observing frequency and over the flux density range 14.5 to 1000 μJy. Over a sky area of diameter 8.2 arcmin corresponding to the one-fourth-power width of the primary beam, $(S_{\mu Jy}/204\ \mu Jy)^{-1.3}$ sources are expected with flux density exceeding $S_{\mu Jy}$. Since zero spacings are not used in the imaging (they contain all the single-dish errors discussed in Section 2.1), the image mean due to the radio sources is expected to be zero. The variance expected in our images due to these radio sources can be estimated as an integral of the differential source count $n(S)$:

$$\nu_S = \int_0^{S_{max}} \int_\theta \int_\phi S^2 |B_{sp}(\theta, \phi)|^2\, n(S)\, dS\, d\theta\, d\phi. \quad (4)$$

This variance varies over the primary beam, and can be computed at any position with an offset (θ_o, ϕ_o) from the centre of the primary beam by using the beam $B_{sp}(\theta, \phi)$, which is the product of the primary beam and the synthesized beam centred at (θ_o, ϕ_o). The integral in equation (4) is performed up to a limiting flux density S_{max} above which we have avoided sources (Section 3). We compute the variance of the confusion noise (σ_S^2) as a weighted average of ν_S over the primary beam, using the square of the primary beam pattern as the weighting function. With no sources subtracted, a low-resolution image made using the short 30.6-m baselines is expected to have an rms confusion noise σ_S in the range 50–130 μJy beam^{-1} (the range refers to the uncertainty in the differential source counts), and this expectation is consistent with the excess rms noise (140 μJy beam^{-1}) estimated to be present in the image in Fig. 2.

4.2 Subtracting discrete source confusion

We have attempted to subtract the discrete foreground radio sources from the brightness-sensitive image (Fig. 2) in order to examine the residual image for possible CMB fluctuations. Previous searches for CMB anisotropy by imaging techniques (Fomalont et al. 1992) have used sensitive images of the field made with much higher angular resolution to detect the discrete radio sources and subtract their effects from the data. However, because the images for detection of confusion are made with interferometer spacings that are several factors larger than the spacings used to detect CMB fluctuations, extended sources that are resolved by the large interferometer spacings would not be properly subtracted. In contrast, we have used the data in the longer three spacings (61.2, 91.8 and 122.4 m) of our compact ATCA array to detect confusion and remove their effects from the 30.6 m baseline data which are used in making the brightness-sensitive image. The rms sensitivity with which we detect confusion would be similar to the sensitivity that the 30.6 m spacing image has for discrete radio sources. The longer baseline data used for detecting confusion are sensitive to source structure on all scales up to, but not including, the scale on which we are attempting to detect structure in the CMB with the brightness-sensitive image. We therefore expect to remove fully the effects of the stronger confusing sources in the field, provided that they do not have angular structure on scales equal to the resolution of our short-spacing image. Moreover, we estimate the strength of confusing sources using interferometers formed from the same antennas that give the short-spacing data. As mentioned earlier, this makes our method relatively insensitive to errors and temporal instabilities in the antenna responses. Although the baselines are formed between the same antennas, the different spacings will have statistically independent instrumental noise (Thompson et al. 1986). The subtraction of a model for the confusion based on the data at longer spacings is thus not expected to decrease the instrumental noise in the short-spacing data, and the residual image will be expected to have the same instrumental noise variance as is present in the raw image in Fig. 2.

We made a CLEAN-deconvolved image using baselines $\gtrsim 61.2$ m (Fig. 3) and found three sources (also seen to be the three sources in Fig. 1) to have flux densities at least a factor of 4 above the image rms noise. We then obtained a three-component model for the confusion in the image by fitting directly to the visibilities on baselines $\gtrsim 61.2$ m. The model was restricted to three components (nine parameters), since there were three components in the image exceeding the noise by four standard deviations, and an increase in the number of parameters would cause the model to include noise peaks with lower standard deviations. The subtraction of confusion would then enhance the rms noise in the short-spacing image. The initial model for the fit consisted of three point components, with nominal flux densities, located at the positions of the three peaks in the long-baseline image. The fit solved for peak values and positions, giving a nine-parameter model for the confusion. The result of the fit was

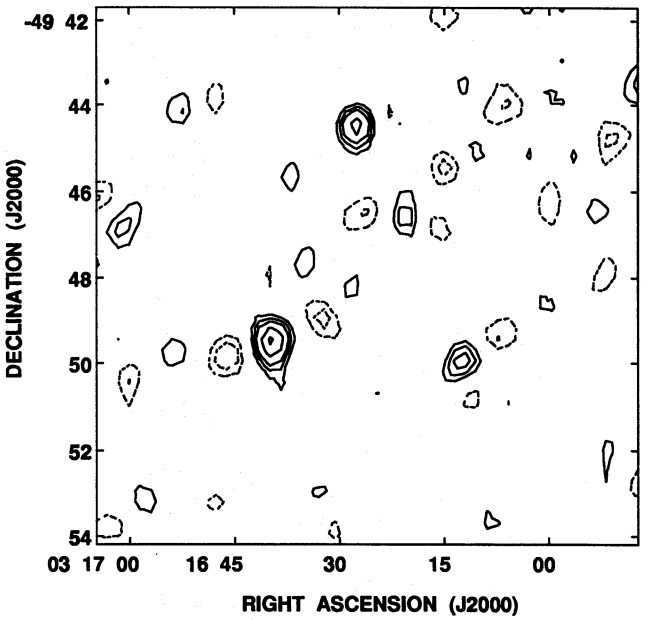

Figure 3. Deconvolved image of the field made using only baselines ≥ 61.2 m. CLEAN components were restored using a Gaussian beam of size 51×45 arcsec^2 at a position angle of $-7°$. Contours are at $-3, -2, 2, 3, 4, 6$ and 8×27 μJy beam^{-1}.

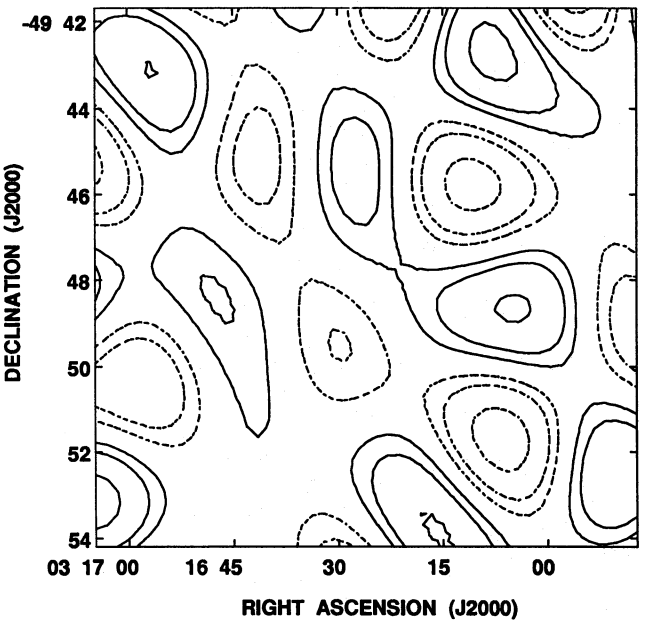

Figure 4. Brightness-sensitive image of the field made using the short 30.6-m baselines after confusion was subtracted from the visibility data. Contours are at $-3, -2, -1, -0.5, 0.5, 1, 2$ and 3×33 μJy beam^{-1}.

three point components with flux densities 224, 186 and 129 μJy at positions close to the three peaks seen in Fig. 3. We then subtracted these components from the 30.6 m baseline visibilities and imaged the residuals. This confusion-subtracted image is shown in Fig. 4. The rms noise in this image in the region of the primary beam is $\sigma_I = 25.5$ μJy beam^{-1}.

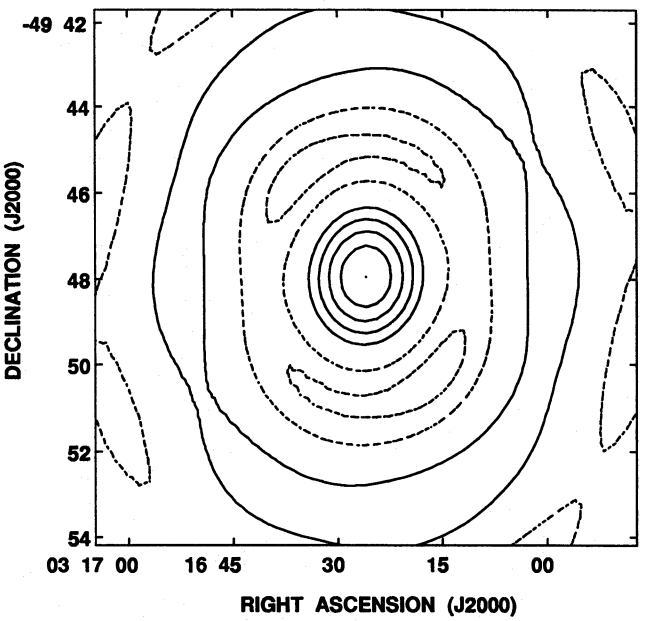

Figure 5. Contour representation of the synthesized beam pattern for the brightness-sensitive image made using the 30.6-m baselines. Contours are at $-40, -20, 20, 40, 60, 80$ and 100 per cent of the peak.

5 UPPER LIMITS ON CMB FLUCTUATIONS

The rms noise (σ_I) in the image in Fig. 4 is consistent with instrumental noise, and we have detected no fluctuations in the background sky. We now use this image to derive upper limits on any fluctuations and then constrain specific models for CMB fluctuation spectra in Sections 5.1 and 5.2.

In an image of the sky made using a Gaussian beam with half-power size $\theta_b \times \phi_b$ arcmin^2, the rms flux density fluctuations in the image ($\Delta S_{\mu Jy}$) can be expressed as rms brightness-temperature fluctuations:

$$\Delta T = 4.5 \left(\frac{8.7\ \mathrm{GHz}}{f_o}\right)^2 \left(\frac{1 \times 1\ \mathrm{arcmin}^2}{\theta_b \times \phi_b}\right) \Delta S_{\mu Jy}\ \mu\mathrm{K}, \qquad (5)$$

where f_o is the observing frequency in GHz. The synthesized beam corresponding to our brightness-sensitive image is shown in Fig. 5 and its half-power size, as determined by a fit of a Gaussian to the main central lobe, is 136×111 arcsec^2. We infer that the rms brightness sensitivity of our image is approximately 36 μK.

The visibilities on all the 30.6-m baselines lie along the same track in the uv-plane. Variations in the rms instrumental noise over the visibility plane will be primarily due to the ≈ 10 per cent change in the antenna system temperatures with elevation. However, if we neglect this small variation and assume the noise to be uniform over the 30.6-m track, the image will be expected to have an instrumental noise distribution with an angular coherence fully determined by the synthesized beam pattern. Intensity fluctuations in the sky, because of discrete radio sources and brightness-temperature variations in any other background radiation, will cause a variance in the visibility data in excess of the instrumental noise. In the image, this excess will be tapered by the primary beam pattern of the telescope antennas. If the sky variance does not vary significantly over the range in

spatial frequencies to which the 30.6-m baseline responds, the spatial coherence of the sky fluctuations in the image will be the same as that for the instrumental noise.

The number of independent sky pixels in the image in Fig. 4 is given approximately by the ratio of the half-power areas of the primary and synthesized beams to be eight. Our Fourier-synthesis image has a zero mean. If we assume the image noise to have a normal distribution and l to be the number of independent sky pixels in the image over which the variance σ_I^2 is estimated, then $l\sigma_I^2$ will have a χ^2 distribution with l degrees of freedom. We simulated images with Gaussian random noise that have a coherence defined by the synthesized beam and obtained the distribution function for the estimator σ_I^2. The distribution is consistent with a number of degrees of freedom $l=10$.

The image in Fig. 4 has $\sigma_I^2=650$ (μJy beam^{-1})^2. We infer the 95 per cent confidence upper limit on the ensemble image variance to be 1625 (μJy beam^{-1})^2. Since this variance is the sum of an instrumental noise contribution of value 1122 (μJy beam^{-1})^2, and any additional sky variance, the 95 per cent confidence upper limit on the rms intensity fluctuations in the background sky is 22 μJy beam^{-1}. Using equation (5), the upper limit to fluctuations in the brightness temperature of the sky at a resolution of 2 arcmin is 25 μK, and the limit on the fractional temperature fluctuations ($\Delta T/T$) in the CMB is 9×10^{-6}.

5.1 Relationship between fluctuations in the sky and image

We may describe the CMB temperature fluctuations on the sky by its angular autocorrelation function $C(\theta)$. The power spectrum of the fluctuations may then be written as a radial transformation:

$$P(Q)=2\pi\int_0^2 \omega C(\omega)J_0(Q\omega)\,\mathrm{d}\omega; \qquad \omega=2\sin(\theta/2). \tag{6}$$

Considering high-order fluctuations on small angular scales, $C(\theta)$ will rapidly approach zero with increasing angle and we can write the power spectrum in the form

$$P(q)=2\pi\int_0^\infty \theta C(\theta)J_0(2\pi\theta\alpha q)\,\mathrm{d}\theta. \tag{7}$$

The Fourier transform conjugate of the sky angle θ, expressed in radians, is the spatial wavelength ψ, which is expressed in wavelengths. We have transformed to the fluctuation wavenumber $q=\psi/\alpha$, where $\alpha=2c/(\Omega_0 H_0)$. q^{-1} has units of Mpc and physically represents the comoving scale of a perturbation at the recombination epoch.

The telescope behaves like a spatial filter that defines the variance at any image position for a specified $P(q)$ on the sky. The telescope filter function (TFF) is obtained by circumferentially averaging the two-dimensional Fourier transformation of the beam pattern $B_{sp}(\theta,\phi)$:

$$F(q)=\int\int B_{sp}(\theta,\phi)J_0(2\pi\alpha q r)\,\mathrm{d}\theta\,\mathrm{d}\phi. \tag{8}$$

The radial angular distance is r and equals $\sqrt{\theta^2+\phi^2}$. Since we work in the spatial frequency domain, we have modelled the primary beam with a physical model for the antenna aperture illumination. Using this model for the primary beam, we have separately computed TFFs using the synthesized beams of (i) the image made using visibilities on the 30.6-m baselines and (ii) the baselines ≥ 61.2 m. We used equation (7) to compute the TFF over a grid of points covering the primary beam, and then averaged the TFFs using the square of the primary-beam pattern as the weighting function. The TFF corresponding to the brightness-sensitive image made using the 30.6-m baselines (continuous line in Fig. 6) peaks around 0.1 Mpc^{-1}. This implies that our experiment has maximum sensitivity to those primary CMB fluctuations which probe structure formation on a comoving scale of 10 h^{-1} Mpc. The sky distribution of CMB temperature is often decomposed using spherical harmonics which are labelled by the order of the multipole k. For the case of small field of view and small angles, we may transform $k=2\pi\alpha q$ and obtain a value $k\approx4500$ as the order of the multipole at which our experimental sensitivity peaks. The TFF for the data used in modelling confusion (dashed line in Fig. 6) is essentially disjoint from the TFF corresponding to the brightness-sensitive image. Most models for CMB fluctuations predict random-phase spectra with no correlation between different angular scales. The independence between the TFFs in Fig. 6 ensures that, after the subtraction of discrete sources, CMB power in the band corresponding to the TFF for the brightness-sensitive image will continue to be present in the residual image as an excess variance.

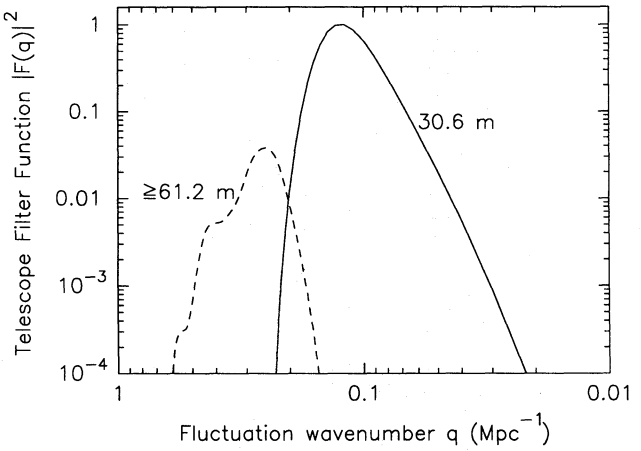

Figure 6. Telescope filter functions corresponding to images made using only the 30.6-m baselines (continuous line) and using baselines ≥ 61.2 m (dashed line). The TFFs have been computed using equation (7) and are plotted as $|F(q)|^2$ versus q with both axes in logarithmic scale.

Using a model power spectrum for the CMB sky, $P(q)$, and the telescope filter function, $F(q)$, we may compute the expected variance in the image as

$$\sigma_C^2=\left(\frac{2k_B}{\lambda^2}\right)^2 2\pi\int_0^\infty qP(q)|F(q)|^2\alpha^2\,\mathrm{d}q\,(\mathrm{Jy\,beam^{-1}})^2. \tag{9}$$

5.2 Limits on Gaussian-model CMB fluctuations

CMB fluctuations may be modelled as having a Gaussian distribution in temperature and a Gaussian-form angular

autocorrelation function

$$C(\theta) = C_o \exp\left(-\frac{\theta^2}{2\theta_c^2}\right), \qquad (10)$$

where $C_o = \langle T^2(\theta)\rangle$ is the variance of the sky brightness and $\theta_c = \sqrt{-C(0)/C''(0)}$ is the coherence scale. The normalized power spectrum for a coherence scale $\theta_c = 1$ arcmin is shown in Fig. 7. The spectrum is seen to be peaked at $q \approx 0.1$ Mpc^{-1}, and has a wider distribution in q-space compared to the TFF of the brightness-sensitive image. Our 95 per cent upper limit on any excess rms in the brightness-sensitive image is 22 μJy beam^{-1}. We compute the expected image rms noise σ_C from equation (9) to be 22 μJy beam^{-1}, provided we assume a value of $C_o = 3000$ (μK)^2 for the CMB variance with a coherence scale of $\theta_c = 1$ arcmin. Therefore our 95 per cent confidence upper limit on $C_0^{1/2}$ is 55 μK, with a corresponding upper limit of 2×10^{-5} on the fractional temperature fluctuations $\Delta T/T$ with the coherence scale $\theta_c = 1$ arcmin.

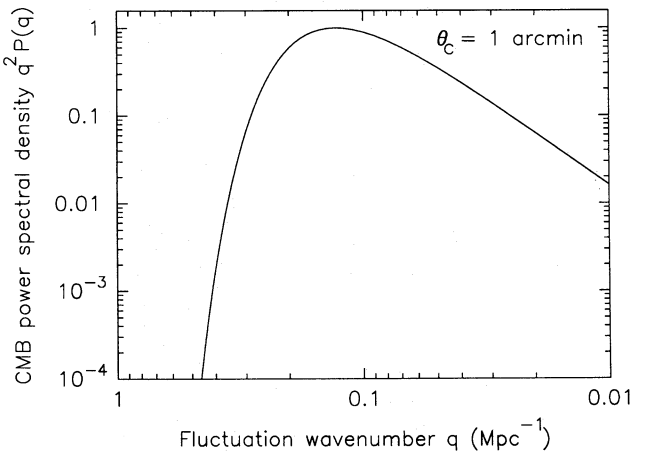

Figure 7. The power spectral density of CMB fluctuations assuming a Gaussian autocorrelation function with coherence scale $\theta_c = 1$ arcmin. The spectrum has been plotted as the power per logarithmic interval, $q^2P(q)$, versus the fluctuation wavenumber q.

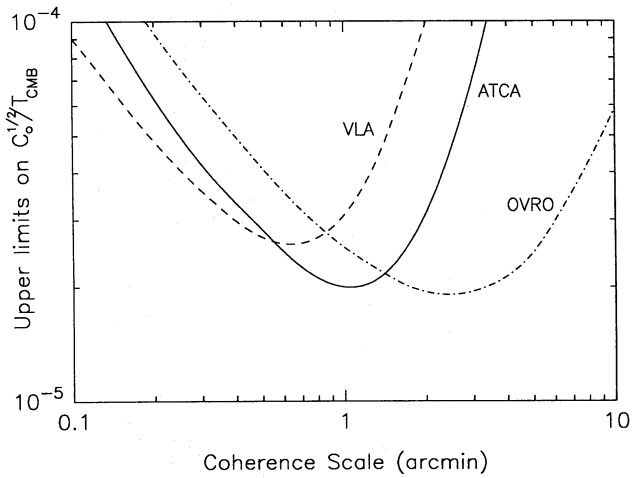

Figure 8. 95 per cent confidence upper limits on the fractional rms fluctuations in the CMB assuming a Gaussian form for the angular autocorrelation function. The results with the ATCA (continuous line) are compared with limits set by Fomalont et al. (1992; dashed line) and Readhead et al. (1989; dot-dashed line).

CMB power spectra with coherence scales offset from 1 arcmin will have a gradation in power across the range in q selected by the TFF. Images can be made to detect these model power spectra optimally by appropriately weighting the visibility data before forming the image. Large changes in the CMB power across the TFF range will also cause the number of degrees of freedom in the variance contribution from the CMB to differ from that in the instrument noise contribution. Since the Gaussian-form power spectra have a wider distribution over fluctuation wavenumbers compared to our telescope filter function, we have assumed that such sky signals have the same fluctuation statistics as the instrumental noise. We then derive 95 per cent confidence limits on Gaussian-model fluctuations over a range of coherence scales (Fig. 8). Upper limits on the fractional temperature fluctuations ($C_0^{1/2}/T_{CMB}$) in the models are plotted against the coherence scale (ϕ_c).

6 A COMPARISON WITH PREVIOUS SEARCHES

A 95 per cent confidence upper limit of $\Delta T/T < 2.1 \times 10^{-5}$ has been claimed for CMB fluctuations on an angular scale of 4 arcmin (Uson & Wilkinson 1984). On 2-arcmin scales, an upper limit of $\Delta T/T < 1.7 \times 10^{-5}$ is claimed with the same confidence (Readhead et al. 1989). An image with 80-arcsec resolution (Fomalont et al. 1992) has been used to derive a limit of $\Delta T/T < 1.9 \times 10^{-5}$ on CMB fluctuations on the 80-arcsec scale. The image we have made using the 30.6-m baselines of the ATCA, with confusion subtracted, has a resolution of about 2 arcmin and places a 95 per cent confidence upper limit of $\Delta T/T < 9 \times 10^{-6}$ on CMB fluctuations on this 2-arcmin scale.

Considering a model CMB fluctuation with a Gaussian form autocorrelation, Readhead et al. derive a 95 per cent confidence limit of $\Delta T/T < 1.9 \times 10^{-5}$ on the model with coherence scale $\theta_c = 2.6$ arcmin. Over the range $22 < \theta_c < 60$ arcsec, Fomalont et al. place an upper limit of $\Delta T/T < 3.0 \times 10^{-5}$, and their best limit is $\Delta T/T < 2.5 \times 10^{-5}$ for $\theta_c = 40$ arcsec. Our imaging experiment is most sensitive to the Gaussian model fluctuations with $\theta_c = 1$ arcmin, and on this scale we place a 95 per cent confidence limit of $\Delta T/T < 2 \times 10^{-5}$. In Fig. 8, the limits placed by the VLA (Fomalont et al. 1992) and the OVRO observations (Readhead et al. 1989) are compared with the ATCA results.

ACKNOWLEDGMENTS

It was a pleasure to attempt this experiment in the jovial and cooperative atmosphere of the Australia Telescope, Narrabri.

REFERENCES

Cole S., Kaiser N., 1988, MNRAS, 233, 637
Fomalont E. B., Partridge R. B., Lowenthal J. D., Windhorst R. A., 1992, ApJ, 404, 8
Franceschini A., Toffolatti L., Danese L., De Zotti G., 1989, ApJ, 344, 35

Haslam C. G. T., Salter C. J., Stoffel H., Wilson W. E., 1982, A&AS, 47, 1
Kraus J. D., 1986, in Radio Astronomy. Cygnus-Quasar Books, Powell, Ohio, pp. 3–42
Large M. I., Mills B. Y., Little A. G., Crawford D. F., Sutton J. M., 1981, MNRAS, 194, 693
Ostriker J. P., Vishniac E. T., 1986, ApJ, 306, L51
Peebles P. J. E., Silk J., 1990, Nat, 346, 233
Peebles P. J. E., Schramm D. N., Turner E. L., Kron R. G., 1991, Nat, 352, 769
Readhead A. C. S. et al., 1989, ApJ, 346, 566
Schaeffer R., Silk J., 1988, ApJ, 333, 509
Smoot G. F. et al., 1992, ApJ, 396, L1
The Australia Telescope, 1992, Special issue of J. Electr. Electron. Eng. Aust., 12, June
Thompson A. R., Moran J. M., Swenson G. W., 1986, Interferometry and Synthesis in Radio Astronomy. Wiley-Interscience, p. 162
Uson J. M., Wilkinson D. T., 1984, Nat, 312, 427
Vittorio N., Silk J., 1984, ApJ, 285, L39
Windhorst R. A., Fomalont E. B., Partridge R. B., Lowenthal J. D., 1993, ApJ, 405, 498
Wright A., Otrupcek R., 1990, Parkes Catalogue, Australia Telescope National Facility, CSIRO